ZIF-67-derived CoO (tetrahedral Co^{2+})@nitrogen-doped porous carbon protected by oxygen vacancies-enriched SnO_2 as highly active catalyst for oxygen reduction and Pt co-catalyst for methanol oxidation

Yang Yu[a], Shijie You[b], Jiannan Du[a], Zipeng Xing[a], Ying Dai[a,c,*], Hun Chen[a], Zhuang Cai[a,*], Nanqi Ren[b], Jinlong Zou[a,*]

[a] Key Laboratory of Functional Inorganic Material Chemistry, Ministry of Education of the People's Republic of China, School of Chemistry and Materials Science, Heilongjiang University, Harbin, 150080, China
[b] State Key Laboratory of Urban Water Resource and Environment, School of Environment, Harbin Institute of Technology, Harbin 150090, China
[c] School of Civil Engineering, Heilongjiang Institute of Technology, Harbin 150050, China

ARTICLE INFO

ABSTRACT

Fabrication of efficient catalyst/co-catalyst for enhancing methanol oxidation and oxygen reduction reactions (MOR/ORR) is the key to make direct methanol fuel cells more economical. Here, hierarchical CoO@nitrogen-doped porous carbon@SnO_2 (CoO@NPC@SnO_2) polyhedrons are prepared as active catalysts for ORR and Pt supports/co-catalysts for MOR using zeolitic imidazolate frameworks-67 (ZIF-67). For ORR, CoO@NPC@SnO_2-1 (Co@NPC-to-$SnCl_2$·$2H_2O$ mass ratio of 1: 1) exhibits a more positive peak potential (0.82 V vs. RHE) than that of commercial Pt/C (10 wt.%). Outer SnO_2 shells can prevent CoO cores (active tetrahedral Co^{2+}) from corrosion during ORR. For MOR, Pt-CoO@NPC@SnO_2-1 (5 wt.%) shows a much higher mass activity (1518 mA mg_{Pt}^{-1}) than that of Pt/C (496.8 mA mg_{Pt}^{-1}). High CO tolerance of Pt-CoO@NPC@SnO_2-1 is attributed to strong metal (Pt)-metal oxides (SnO_2) interactions, which facilitate adsorption of OH^- on SnO_2 to remove CO_{ads}. Therefore, this study provides a strategy to enhance ORR/MOR performance by using hierarchically-structured catalysts/co-catalysts from ZIF templates.

1. Introduction

Direct methanol fuel cells (DMFCs) with high energy density and low operating temperature are environmental friendly energy sources for portable electronic devices and new energy vehicles [1–4]. The working efficiency of DMFCs is mainly determined by two reactions: the oxygen reduction reaction (ORR) of the cathode and the methanol oxidation reaction (MOR) of the anode [5,6]. At present, the most commonly used materials for ORR and MOR are the noble-metal catalysts, especially the platinum (Pt) is an irreplaceably active component for MOR [7]. However, in the cathode, the catalytic activity of Pt-species will be dramatically deteriorated by methanol crossover and carbon monoxide (CO, intermediates) toxicity during ORR [3,7]. Generally, in the anode, the commercial Pt/C catalyst can easily absorb the intermediates (CO, etc) to poison the Pt active sites for MOR, resulting in the severe decline of charge transfer efficiency and mass activity [1,8]. In addition, the expensive price of Pt makes the development of new highly-active and anti-poisoning catalysts more urgent [7,8].

Recently, metal (Co, Fe, Ni, Cu, Sn, etc.) oxides materials have been extensively studied because of their intrinsic catalytic/co-catalytic activity for ORR and MOR (as Pt support) [9,12]. As previously reported, if the metal oxides are embedded in heteroatoms (such as N, P, and B)-doped porous carbon, it can protect the metal oxides from corrosion and agglomeration to obtain a desirable catalytic/co-catalytic activity and long-term stability [8,9]. Masa et al. successfully embed Mn_xO_y and Co_xO_y into the N-doped carbon (NC) structure to obtain the active Mn_xO_y/NC and Co_xO_y/NC catalysts for ORR, respectively [10]. Zhao et al. embed the Mn-Co oxides into N-doped carbon nanotubes (Mn-Co/NCNTs) as ORR catalysts, which exhibit excellent activity and stability for ORR in alkaline media [11]. Sun et al. use carbon dots (CDs) and Co_3O_4 particles as building units to construct the Pt-Co_3O_4-CDs/C composite (12 wt.% Pt), which can enhance the CO-poisoning tolerance and obtain a high catalytic activity of 1393.3 mA mg_{Pt}^{-1} for MOR [12]. These studies prove that the metal oxides embedded in carbon structure can effectively prevent the poisoning of active components, thereby improving the activity and stability of these catalysts for ORR/MOR.

However, the activity and durability of these metal oxides catalysts still has room to be improved to meet the high level of commercial application in the market.

Another efficient approach for obtaining the highly active catalysts is to introduce a special three-dimensional (3d) structure (such as a core-shell structure) to the catalyst [7,9]. Core-shell structure usually possesses the large specific surface area and sufficient exposed active sites, and protects the active cores from deterioration during ORR or MOR [9,13]. Metal-organic frameworks (MOFs) composed of metal ions and organic ligands have become a new platform for synthesis of core-shell structured catalysts due to its unique 3d structure and variable metal elements [14–17]. Among them, zeolitic imidazolate frameworks (ZIFs such as ZIF-67) have better morphology, abundant Co and N species, and large specific surface area, which are usually used as excellent precursors to prepare metal and N co-doped carbon materials (M-N-C) [18,19]. Guo et al. directly carbonize the ZIF-67 to obtain $Co@Co_3O_4@$N-doped carbon polyhedra, which have been used as efficient catalysts for ORR [20]. Aijaz et al. embed the core-shell $Co@Co_3O_4$ nanoparticles in CNT-grafted N-doped carbon-polyhedra obtained from the pyrolysis of ZIF-67 as active ORR catalysts [21]. These catalysts exhibit significantly enhanced catalytic activity towards ORR, which is even comparable to that of Pt-based catalyst, attributing to that the shell (carbon) structure can effectively protect the active cores and skeleton N-species from inactivation [21]. However, the catalytic activity and stability of ZIF-67-derived catalysts still need to be improved. To the best of our knowledge, the formation of 3d structure by annealing ZIF-67 in inert gas for MOR (as Pt support) has not been reported before. From these studies, we find that there is almost no report on the preparation of pure CoO from ZIF-67 for ORR. The tetrahedral Co^{2+} species (Co_{Td}^{2+}) plays a decisive role in catalyzing ORR among all of the Co-species, but CoO is unstable during ORR and may be quickly converted to Co_3O_4 [22–25]. This will result in a decrease of Co^{2+}, even if the Co species is embedded in the carbon skeleton [24]. Therefore, to improve the chemical stability of CoO, it is necessary to further protect the obtained CoO/C with a substance to gain excellent stability and activity for ORR/MOR.

Recently, Huang et al. successfully prepare the highly active and stable SnO_2-covered MWCNTs (MWCNTs@SnO_2) as Pt support/co-catalyst for MOR [13]. Du et al. have prepared the highly stable Pt_{46}-$(SnO_2)_{54}$/C core-shell particles for EOR (ethanol oxidation reaction), and SnO_2 can provide oxophilic species (OH_{ads}) to remove CO_{ads} and $CH_{x,ads}$ [26]. John et al. prepare Pt/Sn nanoparticles with Sn surface coverage of ca. 0.6 and the Sn forms a uniform thin shell of 2D SnO_x on the Pt surface, which can obtain a dramatic improvement in CO_{ads} oxidation ability and a high catalytic activity of 12.5A g_{Pt}^{-1} [27]. These studies demonstrate that SnO_2 can improve the CO poisoning resistance of Pt for MOR/EOR, because it can absorb OH^- species to remove CO_{ads} during the reaction [13,28–30]. Moreover, charges are efficiently transferred from SnO_2 to Pt, because the SnO_2-Pt interactions can improve the electrical conductivity to increase the MOR activity [13,31,33]. Note that SnO_2 as a conductive material with good chemical stability may effectively reduce the conversion of CoO to Co_3O_4 by coating it on the surface of CoO/C, which can simultaneously obtain the high ORR activity and MOR co-catalytic activity [31–33]. These studies inspire us that the cooperation of ZIF-67 (with Co species) and SnO_2 may reveal the promising potential in both ORR and MOR catalysis, which should be explored deeply.

Therefore, we report a two-step pyrolysis-oxidation strategy to synthesize the core-shell structured CoO@N-doped porous carbon@SnO_2 (CoO@NPC@SnO_2) composites as catalysts for ORR and as Pt supports for MOR. The dodecahedral ZIF-67 crystals are prepared as a single precursor to obtain the CoO_x/Co@NPC, and then the surface CoO_x species is washed away by hydrochloric acid (HCl) to obtain the porous Co@NPC with abundant surface oxygen-containing functional groups. Subsequently, the elemental Sn nanoparticles are introduced to cover the Co@NPC surface to obtain a core-shell structured Co@NPC@

Sn material, which is then heated under inert gas condition to obtain the CoO@NPC@SnO_2 with typical 3D bulk networks. CoO@NPC@SnO_2 can be used not only as an ORR catalyst, but also as a Pt co-catalyst/support for MOR. To the best of our knowledge, it is the first time that ZIF-67-derived hierarchical CoO@NPC@SnO_2 composites have been prepared as catalyst/co-catalyst (Pt support) for ORR/MOR. The Co@NPC material still maintains the uniform rhombohedral dodecahedral structure of ZIF-67 after acid pickling, and the surface CoO_x particles are removed to obtain the porous structure in NPC, which should facilitate the mass transfer during the reactions. The surface SnO_2 shells of CoO@NPC@SnO_2 can avoid the fast inactivation (corrosion and agglomeration) of active CoO (Co_{Td}^{2+}) cores during ORR/MOR. Moreover, SnO_2 with good electrical conductivity and abundant oxygen vacancy defects in the crystalline structure can enhance its catalytic activity. The obtained CoO@NPC@SnO_2 (ORR) and Pt-CoO@NPC@SnO_2 (MOR) are expected to exhibit higher activity, durability and methanol/CO_{ads} tolerance than those of commercial Pt/C in alkaline media.

2. Experimental

### 2.1. Preparation of ZIF-67 polyhedrons and Co/NPC

ZIF-67 was prepared according to a previously reported synthesis method [7]. $Co(NO_3)_2 \cdot 6H_2O$ (291 mg) was dissolved in 25 mL of methanol to obtain solution A. 2-methylimidazole (328 mg) was also dissolved in 25 mL of methanol to obtain solution B. Then, the solution B was quickly poured into the solution A under vigorous agitation for 20 min. The well mixed solution was aged for 24 h without stirring at room temperature (25 °C). Finally, purple precipitate (ZIF-67) was washed with absolute methanol for four times, which was then dried in a vacuum oven at 60 °C overnight. The CoO_x/Co@NPC was obtained by annealing ZIF-67 polyhedrons under N_2 atmosphere at 700 °C for 2 h at a heating rate of 2 °C min^{-1}. Acid pickling (3 M HCl, 30 min) was used to remove the CoO_x components from the CoO_x/Co@NPC sample. The sample was washed with deionized water for several times, which was then dried in a vacuum oven at 60 °C overnight to obtain Co@NPC.

2.2. Preparation of CoO@NPC@SnO_2

The obtained Co@NPC was immersed in a mixed solution of $SnCl_2 \cdot 2H_2O$ and methanol (20 mL), and sonicated for 30 min. Then, excessive $NaBH_4$ was added to the mixture solution under vigorous stirring at room temperature (25 °C) for 1 h. The products were washed with absolute methanol for several times, which was then dried in a vacuum at 60 °C overnight to obtain the Co@NPC@Sn. The CoO@NPC@SnO_2 was obtained by directly annealing the Co@NPC@Sn sample under N_2 atmosphere at 800 °C for 2 h at a heating rate of 2 °C min^{-1}. CoO@NPC@SnO_2 samples with Co@NPC-to-$SnCl_2 \cdot 2H_2O$ mass ratio of 1: 0.5, 1: 0.75, 1: 1, 1: 1.25 and 1: 1.5 were marked as CoO@NPC@SnO_2-y (y = 0.5, 0.75, 1, 1.25 and 1.5). The CoO@NPC was also prepared by directly annealing the Co@NPC after acid pickling without introduction of Sn.

2.3. Preparation of Pt-CoO@NPC@SnO_2

Pt-CoO@NPC@SnO_2 catalysts with 5 wt.% Pt were prepared by liquid phase reduction method. The obtained CoO@NPC@SnO_2 was immersed in $H_2PtCl_6 \cdot 6H_2O$ solution with 30 min sonication. Then, pH of the mixture was adjusted to 10 by using 1 M NaOH solution. Pt-species (elemental Pt nanoparticles) was slowly reduced by dropwisely adding the excessive sodium borohydride solution to the above suspension with vigorous stirring. The mixture was continuously stirred for 3 h and then allowed to stand for at least 12 h at room temperature (25 °C). The Pt-CoO@NPC@SnO_2 was collected by centrifugation (4000 rpm), which was then washed with deionized water and absolute ethanol
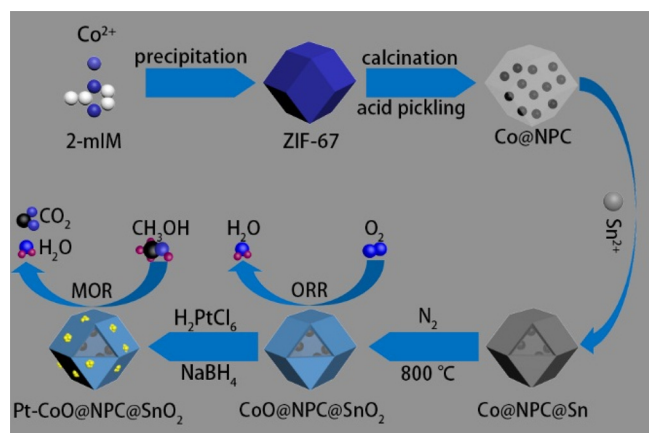
Scheme 1. Synthesis route for CoO@NPC@SnO$_2$ and Pt-CoO@NPC@SnO$_2$ composites.

several times and dried in a vacuum oven at 60 °C overnight. The Pt-CoO@NPC (5 wt.%) was also prepared by using the same method as mentioned above. The mass percentages of Pt in Pt-CoO@NPC@SnO$_2$ and Pt-CoO@NPC catalysts were determined by using Inductively Coupled Plasma Atomic Emission Spectrometer (ICP-AES, Optima 7000DV). As shown in Table S1, the calculated values were very close to the theoretical Pt content and thus 5 wt.% was used for various calculations in the following tests. The schematic synthesis procedure was shown in Scheme 1. The information for material characterizations including X-ray powder diffraction (XRD), X-ray photoelectron spectroscopy (XPS), scanning electron microscope (SEM), elemental mappings by using energy-dispersive X-ray spectroscopy (SEM-EDS) and transmission electron microscopy (TEM) were provided in

'Supplementary Information'. The information for electrochemical measurements including cyclic voltammetry (CV), linear sweep voltammetry (LSV), accelerated durability test (ADT), electrochemical impedance spectroscopy (EIS), chronoamperometry (CA), rotating disk electrode (RDE) and rotating ring disk electrode (RRDE) were also provided in 'Supplementary Information'.

3. Results and discussion

3.1. Characteristics and structure of (Pt)CoO@NPC@SnO$_2$

Fig. S1a shows the XRD patterns of ZIF-67 and all of the diffraction peaks are the same as the standard ZIF-67 reported in previous study [34]. As shown in Fig. 1a, the XRD patterns of carbonized ZIF-67 at 700 °C under N$_2$ atmosphere show the diffraction peaks at around 44.2°, 51.5°, and 75.9°, corresponding to the (111), (200) and (220) planes of Co^0 (JCPDS, NO.15-0806), respectively [21]. The diffraction peaks at around 19°, 31.27°, 36.84°, 59.36°, and 65.24° correspond to the (111), (220), (311), (511) and (440) planes of Co$_3$O$_4$ (JCPDS, NO.42-1467), respectively [35]. The diffraction peaks at around 36.5°, 42.4° and 61.52° correspond to the (111), (200) and (220) planes of CoO (JCPDS, NO.43-1004), respectively [36]. The diffraction peak at around 26° correspond to the (002) plane of graphitic carbon, suggesting that the Co species (Co^0, Co$_3$O$_4$, and CoO) in carbonized ZIF-67 has the catalytic activity to convert the amorphous carbon to graphitic (or partly graphitized) carbon [37]. As shown in Fig. 1b, the diffraction peaks of the CoO$_x$ species disappear, indicating that only the CoO$_x$ species in the structure is removed after acid pickling, and most of the graphitic carbon-protected Co is not removed. As shown in Fig. 1c, the diffraction peaks at around 26.61°, 33.89°, 37.94°, 38.97°, 51.78°, 54.76°, 57.82°, 61.87°, 64.72°, 65.94°, 71.28° and 78.71° correspond to the (110), (101), (200), (111), (211), (220), (002), (310), (112), (301), (202) and
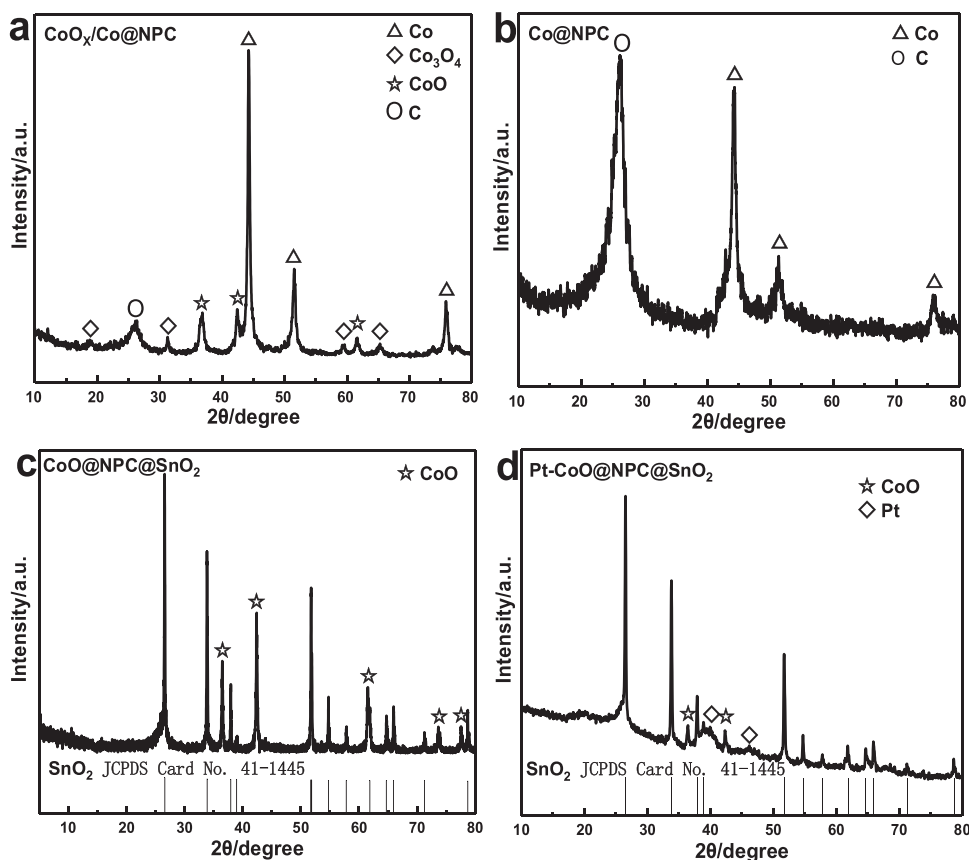
Fig. 1. XRD patterns of the CoO$_x$@NPC (a), Co@NPC (b), CoO@NPC@SnO$_2$ (c), and Pt- CoO@NPC@SnO$_2$ (d).
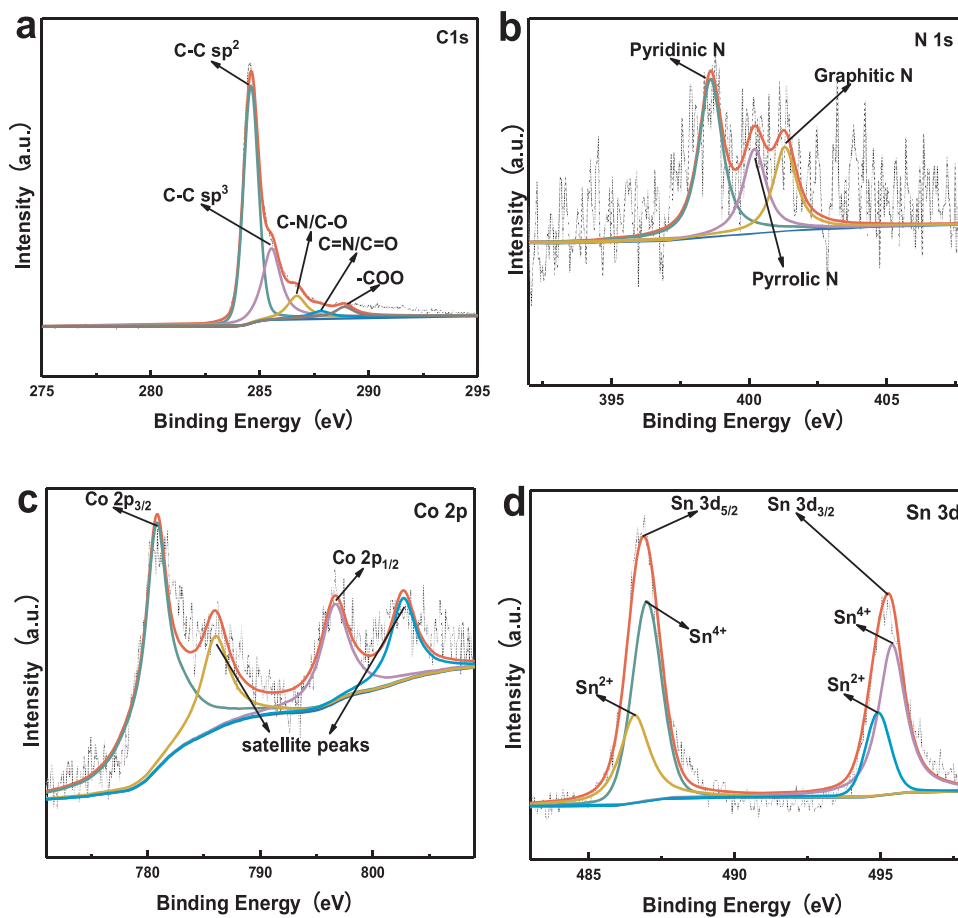
Fig. 2. High resolution XPS spectra of C 1s (a), N 1s (b), Co 2p (c) and Sn 3d (d) for CoO@NPC@SnO$_2$-1.

(321) planes of SnO$_2$ (JCPDS, NO.41-1445), respectively. Other obvious diffraction peaks at around 36.5°, 42.4° and 61.52° are assigned to the (111), (200) and (220) planes of CoO (JCPDS, NO.43-1004), respectively, demonstrating that CoO@NPC@SnO$_2$ is successfully obtained [13,36]. Fig. 1d shows that the diffraction peaks at around 39.8° and 46.2° correspond to the (111) and (200) planes of Pt (JCPDS, NO.04-0802), respectively, while the other diffraction peaks correspond to SnO$_2$ (JCPDS, NO.41-1445) or CoO (JCPDS, NO.43-1004) [8,36]. As shown in Fig. S1b, the obvious diffraction peaks at around 36.5°, 42.4°, 61.52°, 73.70° and 77.56° are assigned to the (111), (200), (220), (311) and (222) planes of CoO (JCPDS, NO.43-1004), respectively, demonstrating the successful preparation of CoO@NPC.

As shown in Fig. S2, N$_2$ adsorption/desorption tests are conducted to obtain the specific surface area (S$_{BET}$) and pore size of the as-prepared catalysts. All of the adsorption-desorption isotherms of CoO@NPC@SnO$_2$-y show the type-IV (at p/p$_0$ = 0.45) hysteresis loops, indicating the existence of mesopores [38]. The pore size distributions also indicate that most of the pores are between 2 and 10 nm in diameter, which is big enough for free diffusion of O$_2$ with the kinetic diameter of 0.346 nm [14,38]. The S$_{BET}$ of CoO$_x$/Co@NPC and CoO@NPC@SnO$_2$-y (y = 0.5, 0.75, 1.0, 1.25 and 1.5) are 203.13, 395.3, 383.58, 311.19, 293.89, 290.98 m^2 g^{-1}, respectively. It can be observed that S$_{BET}$ gradually decreases with the increase of SnCl$_2$·2H$_2$O content. This result indicates that excessive SnO$_2$ should block the pore channels in the CoO@NPC structure to lower the S$_{BET}$ of the as-prepared materials. Note that S$_{BET}$ of the as-prepared CoO@NPC@SnO$_2$ are larger than that of the carbonized ZIF-67 (with Co species) as previously reported, indicating that after acid pickling, the CoO$_x$ nanoparticles embedded in the carbon skeleton are desirably removed to obtain the pore structure and bigger S$_{BET}$ [14].

As shown in Figs. 2 and S3, the XPS survey spectra reveals that Co, Sn, N, O and C elements are co-existed on the surface of CoO@NPC@SnO$_2$-1. Fig. 2a shows the high-resolution XPS spectra of C1 s. Five peaks located at around 284.6, 285.6, 286.7, 287.8 and 288.9 eV correspond to C − C sp^2, C − C sp^3, C − N/C − O, C = N/C = O and –COO, respectively [38]. The high peak intensity of the C − C sp^2 indicates that the CoO@NPC@SnO$_2$-1 has a high degree of graphitization. The existence of C–N/C–O and C=N/C=O proves that the N is successfully doped into the carbon skeleton. As shown in the high-resolution XPS spectra of N 1s (Fig. 2b), three peaks located at around 398.6, 400.2 and 401.3 eV correspond to pyridinic N, pyrrolic N and graphitic N, respectively. According to previous studies, pyridinic N and graphitic N can effectively boost ORR activity [39]. Pyridinic N has the ability to lower the energy barrier of O$_2$ adsorption on adjacent C atoms to enhance the charge transfer for ORR [39]. Graphite N can attract electrons from adjacent C atoms to improve the oxygen adsorption on carbon skeleton [39]. As shown in Fig. 2c, the Co 2p spectrum shows two typical peaks at around 780.7 and 796.6 eV, corresponding to Co 2p$_{3/2}$ and Co 2p$_{1/2}$, respectively, and the other two relatively significant peaks at around 786.0 and 802.7 eV are the satellite peaks, which correspond to Co^{2+} (Co$_{Td}^{2+}$) in CoO [40]. As previously reported, the Co^{2+} in CoO@NPC@SnO$_2$ should contribute to the promising catalytic activity for ORR [22–25].

As shown in Fig. 2d, the peaks located at around 486.3 and 494.7 eV correspond to Sn^{2+}, while the peaks at around 486.8 and 495.1 eV correspond to Sn^{4+}. Both Sn^{4+} and Sn^{2+} species are detected in CoO@NPC@SnO$_2$, indicating that the oxygen vacancies are successfully introduced to SnO$_2$ after annealing [41]. According to previous studies, SnO$_2$ with good chemical stability and electrical conductivity can enhance the charge transfer to resist methanol/CO$_{ads}$ poisoning
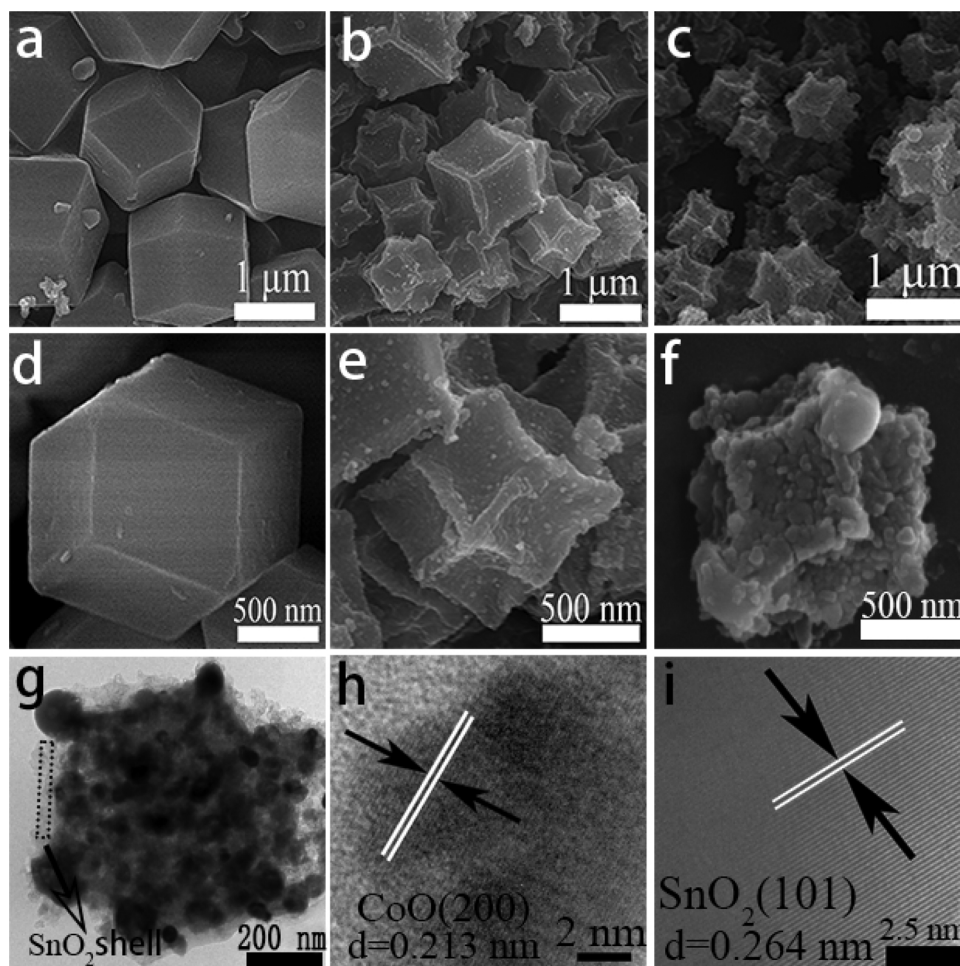
Fig. 3. SEM images of the ZIF-67 (a and d), Co@NPC (b and e), CoO@NPC@SnO$_2$-1(c and f); TEM images of CoO@NPC@SnO$_2$-1 (g) and HRTEM images of CoO@NPC@SnO$_2$-1 (h and i).

[13,29,32,42]. Moreover, a strong metal-metal oxide interaction between SnO$_2$ and Pt can increase the electron density of local Pt nanoparticles to increase the MOR activity [31,33]. As shown in Fig. S3, five typical peaks located at around 530.6, 531.1, 531.9, 532.5 and 533.6 eV are found in O 1s spectrum [38,41]. The energy at around 530.6 eV corresponds to oxygen bound to metal in the crystal lattice of metal oxides (denoted as O$_\alpha$) [41]. The peak at around 531.9 eV corresponds to nonstoichiometric oxygen, including oxygen-deficient regions caused by oxygen vacancies, oxygen interstitials, and oxygen antisites (denoted as O$_\beta$) [41]. The existence of oxygen vacancies can improve the adsorption of oxygen to improve ORR catalytic activity. The binding energies at around 531.1, 532.5 and 533.6 eV are attributed to the oxygen-containing functional groups (C=O, C−O, and −COO) [38]. This result indicates that the surface oxygen-containing functional groups are generated on the carbon skeleton after the acid pickling. The oxygen-containing functional groups can promote the oxygen adsorption, thereby improving the ORR catalytic activity [38,43]. Fig. S8 shows the Pt high resolution XPS spectra of Pt-CoO@NPC and Pt-CoO@NPC@SnO$_2$-y (y = 0.5, 0.75, 1.25 and 1.5). The peaks located at around 71.6 and 74.8 eV correspond to Pt^0, while the peaks at around 72.6 and 75.9 eV correspond to Pt^{2+}. The binding energies of Pt 4f of Pt-CoO@NPC@SnO$_2$ catalysts have negative shifts of 0.1–0.8 eV by comparing with that of Pt-CoO@NPC, implying that there are a strong metal (Pt)-metal oxide (SnO$_2$) interactions and a partial electron transfer from SnO$_2$ to Pt [13]. The high resolution XPS spectra of C 1s, N 1s, Co 2p, Sn 3d and O 1s for CoO@NPC@SnO$_2$-y (y = 0.5, 0.75, 1.25 and 1.5) are shown in 'Supplementary Information'.

Fig. 3a and d show the SEM images of the prepared ZIF-67 template. The as-prepared ZIF-67 has the uniformly rhombic dodecahedral morphology with a particle size of approximately 1 μm. As shown in Fig. 3b and e, the as-prepared Co@NPC retains the rhombic dodecahedral morphology of ZIF-67. However, the particle size of Co@NPC (approximately 1 μm) slightly decreases due to the consumption of imidazolate ligand during pyrolysis at high temperatures, and some N atoms in the imidazolate ligand form the C−N/C=N bonds, consistent with XPS results [20]. As shown in Figs. 3c, f and S9, the CoO@NPC@SnO$_2$-y (y = 0.5, 0.75 and 1.0) well retains the rhombic dodecahedral morphology, indicating that the proper content of SnO$_2$ does not influence the CoO@NPC@SnO$_2$ morphology. However, the CoO@NPC@SnO$_2$-y (y = 1.25 and 1.5) lose the original rhombic dodecahedral morphology, attributing to that the formed SnO$_2$ shells are too thick to cover the morphology completely. Meanwhile, the thick SnO$_2$ shells will greatly reduce the S$_{BET}$ of as-prepared materials, consistent with S$_{BET}$ results. The SEM-EDS elemental mappings reveal that N, O, Co and Sn (Pt) elements are uniformly distributed on the surfaces of CoO@NPC@SnO$_2$ (Fig. S10) and Pt-CoO@NPC@SnO$_2$ (Fig. S11) particles. As shown in the TEM image of CoO@NPC@SnO$_2$-1 (Fig. 3g), the particle with a diameter of ~1 μm has the dense inner cores (CoO@C) and the thin outer shells (SnO$_2$). As shown in Fig. 3h and i, the lattice spacing of 0.264 nm (surface) and 0.213 nm (shallow part) correspond to (101) plane of SnO$_2$ and (200) plane of CoO, respectively, consistent with XRD results. Both SEM-EDS elemental mappings and TEM images prove that the prepared CoO@NPC@SnO$_2$ has a core-shell structure. As shown in Fig. S12a (TEM image), the Pt-CoO@NPC@SnO$_2$-1 still
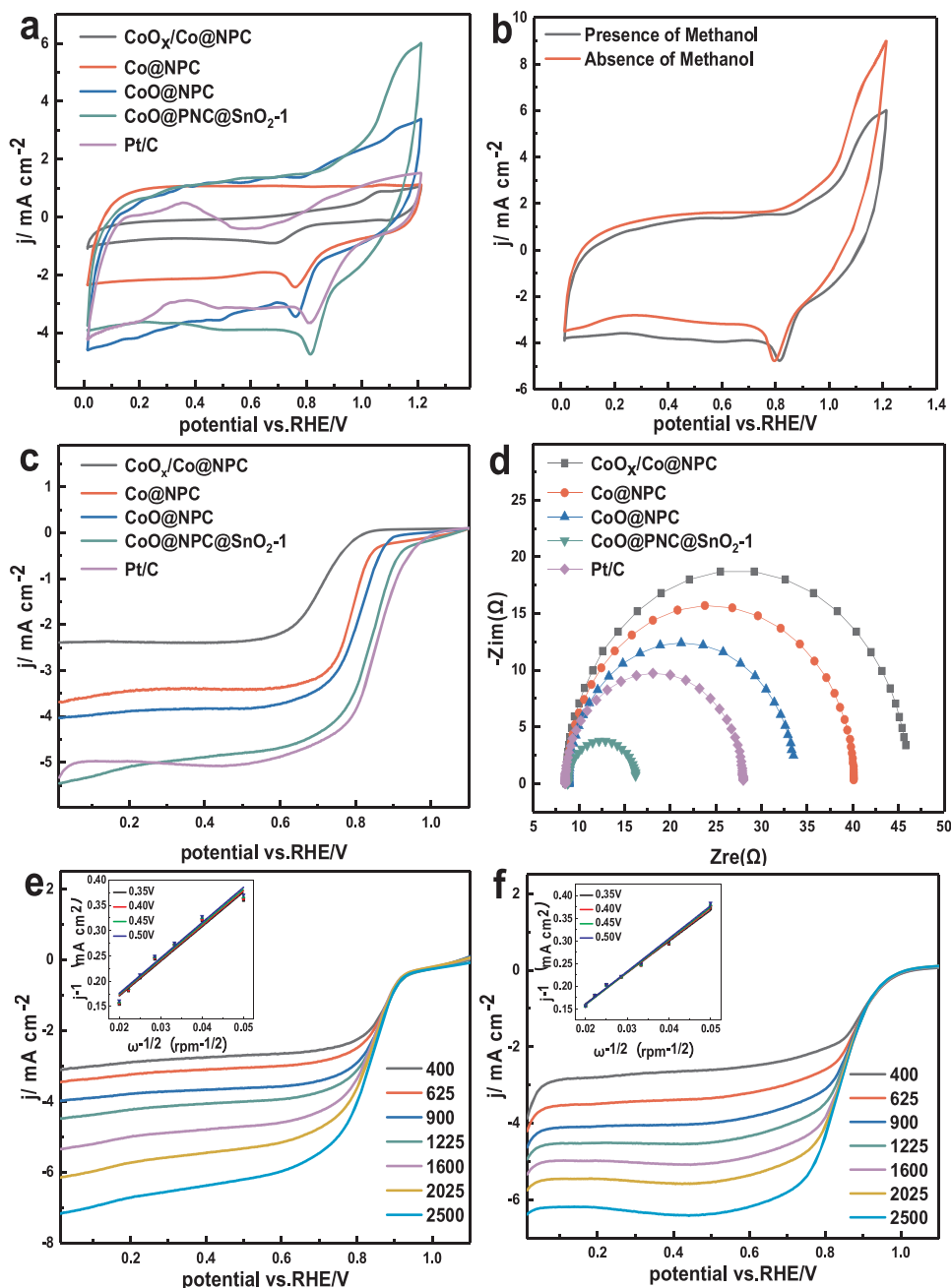
Fig. 4. CV curves of CoO$_x$/Co@NPC, Co@NPC, CoO@NPC, CoO@NPC@SnO$_2$-1 and Pt/C catalysts in O$_2$-saturated 0.1 M KOH solution at a scan rate of 50 mV s^{-1} (a); CV curves of CoO@NPC@SnO$_2$-1 in 0.1 M KOH solution with or without 1 M methanol (b); LSV curves (5 mV s^{-1}) (c) and Nyquist curves (d) of CoO$_x$/Co@NPC, Co@NPC, CoO@NPC, CoO@NPC@SnO$_2$-1 and Pt/C catalysts in O$_2$-saturated 0.1 M KOH solution at 1600 rpm; LSV curves and calculated K–L plots at different potentials (insets) of CoO@NPC@SnO$_2$-1 (e) and Pt/C (f) in O$_2$-saturated 0.1 M KOH at different RDE rotation rates (5 mV s^{-1}).

retains the original morphology of CoO@NPC@SnO$_2$-1 after Pt loading. Fig. S12b shows the high resolution TEM image of Pt-CoO@NPC@SnO$_2$-1, and a large number of small particles (Pt) are uniformly dispersed on the catalyst surface. As shown in Fig. S12c, the lattice spacing of 0.226 nm corresponds to (111) plane of Pt.

3.2. ORR activity of CoO@NPC@SnO$_2$-y catalysts

CV tests are used to evaluate the ORR performances of Pt/C, CoO$_x$/Co@NPC, Co@NPC, CoO@NPC and CoO@NPC@SnO$_2$-y (y = 0.5, 0.75, 1.0, 1.25 and 1.5). As shown in Figs. 4a and S13, all of the catalysts show well-defined reduction peaks with obviously quasi-rectangular voltammogram in O$_2$-saturated 0.1 M KOH solution. The area of quasi-

rectangular voltammogram of CoO@NPC@SnO$_2$-1 is much larger than those of Pt/C, CoO@NPC and other CoO@NPC@SnO$_2$ catalysts. Generally, the larger the area of quasi-rectangular voltammogram is, the larger the electrochemical active area is [44]. As y increases, the potentials of reduction peak in the CV curves first shift positively and then shift negatively. CoO@NPC@SnO$_2$-1 has the most positive peak potential (0.82 V), which is 20 mv larger than that of Pt/C (0.8 V) and 140 mv larger than that of CoO$_x$@NPC (0.68 V), attributing to that the 3d mesoporous structure facilitates the fast mass transport of ORR-relevant species (O$_2$, H$_2$O, and OH$^-$) to thus improve the ORR activity [14,45]. Fig. S14 shows the CV curves of CoO@NPC@SnO$_2$-1 in N$_2$ or O$_2$ saturated electrolyte, further demonstrating that the promising reduction peak is an O$_2$ reduction peak. Fig. 4b shows the CV curves in O$_2$-
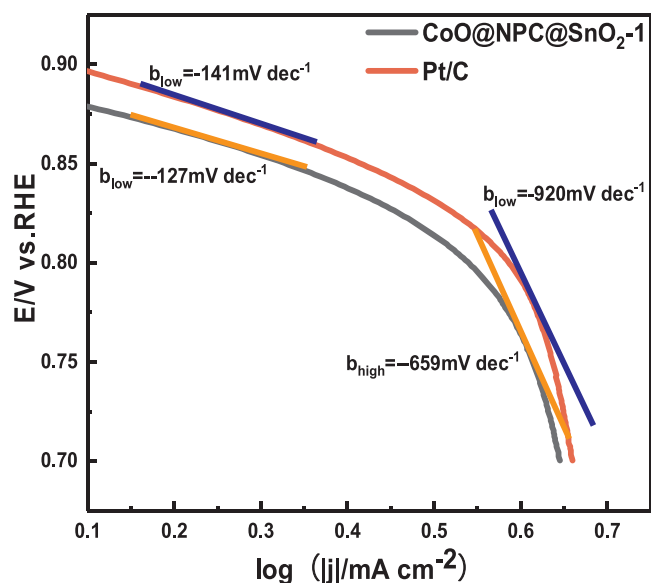
Fig. 5. Tafel plots of the CoO@NPC@SnO$_2$-1 and Pt/C calculated from the results in Fig. 4c.

saturated 0.1 M KOH solution with or without 1 M methanol to investigate the methanol tolerance property of CoO@NPC@SnO$_2$-1. With 1 M methanol, the CV curve of Pt/C shows a significant methanol oxidation peak at the potential of 0.8 V (Fig. S15), while the oxygen reduction peak of CoO@NPC@SnO$_2$-1 almost has no change, indicating that CoO@NPC@SnO$_2$-1 has a promising tolerance to methanol crossover.

To further investigate the ORR performances of CoO@NPC@SnO$_2$ catalysts, LSV tests are performed in an O$_2$-saturated 0.1 KOH solution at 1600 rpm. As shown in Figs. 4c and S16, the CoO@NPC@SnO$_2$-1 exhibits the best ORR performance with the onset potential (E$_O$) of 0.95 V, half-wave potential (E$_{1/2}$) of 0.83 V and limiting current density (J$_L$) of −5.5 mA cm^{-2}. Its ORR performance is better than those of CoO$_x$/Co@NPC (E$_O$ = 0.88 V, E$_{1/2}$ = 0.71 V and J$_L$ = −2.4 mA cm^{-2}), Co@NPC (E$_O$ = 0.89 V, E$_{1/2}$ = 0.78 V and J$_L$ = −3.7 mA cm^{-2}) and CoO@NPC (E$_O$ = 0.91 V, E$_{1/2}$ = 0.80 V and J$_L$ = −4.1 mA cm^{-2}), and comparable to that of Pt/C (E$_O$ = 1.0 V, E$_{1/2}$ = 0.84 V and J$_L$ = −5.3 mA cm^{-2}). Summary of the ORR activities of CoO@NPC@SnO$_2$-1 and other recently-reported catalysts is listed in Table S2 [45–54]. The high catalytic activity of CoO@NPC@SnO$_2$-1 for ORR can be attributed to its high contents of Co$_{Td}^{2+}$, oxygen-containing functional groups (C=O, C—O, and −COO) and N species (pyridinic N and graphitic N) in the carbon skeleton [20,22,38]. The surface Co$_{Td}^{2+}$ species with a neighboring oxygen vacancy is the real active sites, which can promote the O$_2$adsorption/activation (the rate-determined step of ORR) during ORR [9]. As previously reported, the presence of oxygen vacancy can act as the adsorption sites to accelerate the adsorption of oxygen molecules, meanwhile the active Co$_{Td}^{2+}$ sites facilitate the dissociation of oxygen molecules to reduce O$_2$ more easily to produce H$_2$O, consequently favoring the direct 4e$^-$ reaction pathway from O$_2$ to OH$^-$ on the CoO@NPC@SnO$_2$ surface [24,55–57]. The surface Co^{2+} (CoO) can also transfer electrons to the O$_2$ absorbed on the active sites to weaken and break the O − O bond [23]. Moreover, the porous structure (high S$_{BET}$) is favorable to expose more active sites in CoO@NPC@SnO$_2$-1 to lower the reaction resistance to improve the ORR activity, consistent with CV results [14,38]. Nyquist plots of CoO@NPC@SnO$_2$ and Pt/C catalysts are obtained in a frequency range of 100 kHz − 100 mHz in O$_2$-saturated 0.1 M KOH solution at 1600 rpm (inset is the equivalent circuit diagram). As shown in Figs. 4d and S17, the charge transfer resistance (R$_{ct}$, 7.5 Ω) of CoO@NPC@SnO$_2$-1 is the smallest one among all of the catalysts, demonstrating that the CoO@

NPC@SnO$_2$-1 can obtain the fast faradaic process and promising charge transfer kinetics for ORR. The smaller R$_{ct}$ of CoO@NPC@SnO$_2$-1 is partly due to the high electrical conductivity of SnO$_2$ and NPC [32].

ORR kinetics and electron transfer number (n) of CoO@NPC@SnO$_2$-1 and Pt/C are investigated by RDE tests in an O$_2$-saturated 0.1 M KOH solution. Fig. 4e and f show that the disk current densities of CoO@NPC@SnO$_2$-1 and Pt/C gradually increase as the electrode rotation rate increases. According to previous report, there are two kinds of reaction pathways for ORR: 2e$^-$ and 4e$^-$ pathways [52]. As shown in Fig. S18, the electron transfer number of CoO@NPC@SnO$_2$-1 and Pt/C calculated by Koutecky-Levich (K–L) equation are close to the theoretical value of 4.0 at various potentials from 0.35 to 0.50 V [38]. This result indicates that both CoO@NPC@SnO$_2$-1 and Pt/C conduct the ORR via the 4e$^-$ pathway. RRDE tests are also conducted to confirm this result by monitoring the peroxide species (H$_2$O$_2$) yield [50]. As shown in Fig. S19, CoO@NPC@SnO$_2$-1 has 5.6 to 7.2% H$_2$O$_2$ yields over a wide potential range from 0.0 to 0.7 V, with n ranging from 3.843 to 3.876 in 0.1 M KOH solution, suggesting that the ORR process of CoO@NPC@SnO$_2$-1 has a high selectivity for generating OH$^-$ as the main product. This result is consistent with the RDE results, further demonstrating that ORR is performed via a 4e$^-$ pathway in alkaline electrolyte on CoO@NPC@SnO$_2$-1. The favorable 4e$^-$ reduction is mainly due to the Co$_{Td}^{2+}$ and abundant oxygen vacancies with disordered structural layer in SnO$_2$, which can act as adsorption sites for oxygen ion and/or water to improve the mass transfer efficiency [58]. Moreover, oxygen vacancies can also act as the electron donors to improve charge transfer during ORR [59].

For further study the ORR kinetics of CoO@NPC@SnO$_2$-1 and Pt/C. Fig. 5 shows the Tafel plots of CoO@NPC@SnO$_2$-1 and Pt/C, both of which show the typical two-stage linear regions in low- and high-current-density ranges from 0.1 to 0.66 and from 0.7 to 0.9 in the logarithmic scale, respectively. It shows that CoO@NPC@SnO$_2$-1 and Pt/C have similar switches from the Temkin to Langmuir mechanism for oxygen adsorption. The lower the slope of Tafel curve is, the higher the catalytic activity and the reaction kinetics are [38]. CoO@NPC@SnO$_2$-1 (127 mV dec^{-1} and 659 mV dec^{-1}) and Pt/C (141 mV dec^{-1} and 920 mV dec^{-1}) possess similar slopes in the above-mentioned two regions, indicating that CoO@NPC@SnO$_2$-1 and Pt/C have similar ORR kinetics, consistent with the results of n values and RRDE.

CA tests are implemented to evaluate the ORR durability of CoO@NPC@SnO$_2$-1, Co@NPC, CoO@NPC and Pt/C. As shown in the i-t curves (Fig. 6a), after 30,000 s, the retained percentages of current densities for CoO@NPC@SnO$_2$-1, Co@NPC, CoO@NPC and Pt/C electrocatalysts are 72.8, 60.4, 61.8, and 45.6%, respectively. The CA results indicate that CoO@NPC@SnO$_2$-1 has a higher durability for ORR. As shown in Fig. 6b, the i–t curve of CoO@NPC@SnO$_2$-1 almost has no change after adding 1 M methanol at 400 s, while the current density of Pt/C appears a sharp jump (MOR). It indicates that CoO@NPC@SnO$_2$-1 has an excellent methanol tolerance. As shown in Fig. S20a (i–t curves), both CoO@NPC@SnO$_2$-1 and CoO@NPC have observable declines in the current densities after the addition of 1 M methanol at 400 s. However, the decline of current density of CoO@NPC is significantly greater than that of CoO@NPC@SnO$_2$-1. Figs. 6c, d and S20b show that the E$_{1/2}$ of CoO@NPC@SnO$_2$-1 negatively shifts 10 mV after 5000 cycles, which is 2.0 and 3.0 mV smaller than those of Pt/C and CoO@NPC (ADT tests), respectively. CA and ADT tests together demonstrate that CoO@NPC@SnO$_2$-1 has excellent stability and methanol tolerance for ORR, attributing that the SnO$_2$ shells and porous carbon skeleton jointly prevent the highly active CoO (Co$_{Td}^{2+}$) from corrosion and aggregation [7,9].

3.3. MOR activity of Pt-CoO@NPC@SnO$_2$-y catalysts

CV tests are used to evaluate the methanol oxidation performances of Pt-CoO@NPC@SnO$_2$-y and Pt/C. Fig. S21 shows the ECSAs of Pt-CoO@NPC@SnO$_2$-1 and Pt/C in 1 M KOH solution. The
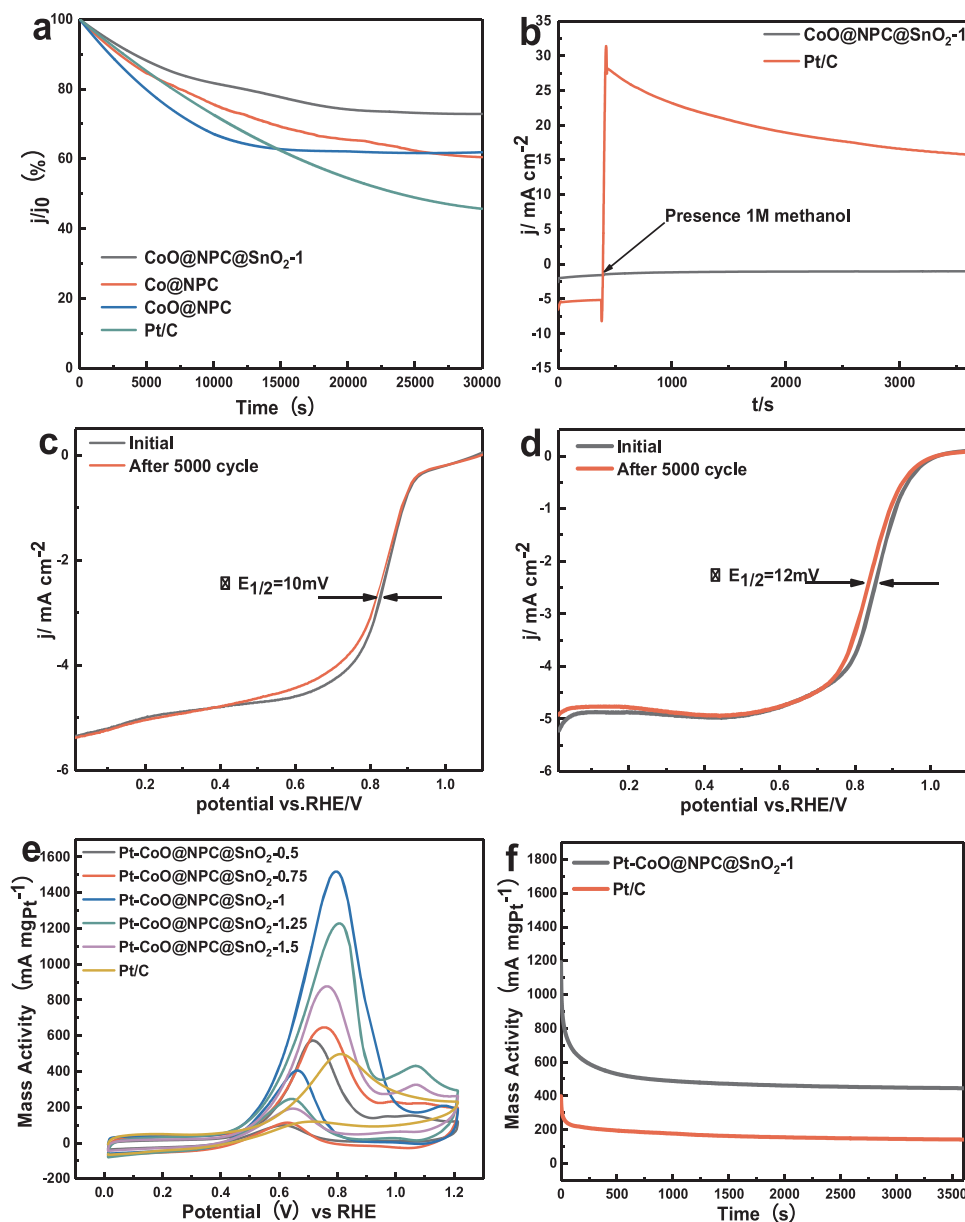
Fig. 6. i–t curves of CoO@NPC@SnO$_2$-1, Co@NPC, CoO@NPC and Pt/C in the O$_2$-saturated 0.1 M KOH at 1600 rpm (a); i–t curves of CoO@NPC@SnO$_2$-1 and Pt/C before and after the addition of 1 M methanol (b); ORR polarization curves of CoO@NPC@SnO$_2$-1 (c) and Pt/C (d) before and after the continuous operation in the O$_2$-saturated 0.1 M KOH at 1600 rpm; CV curves of Pt-CoO@NPC@SnO$_2$ and Pt/C catalysts in 1 M KOH with 1 M methanol at a scan rate of 50 mV s^{-1} (e); CA curves of Pt-CoO@NPC@SnO$_2$-1 and Pt/C in 1 M KOH with 1 M methanol (f).

electrochemically active surface area (ECSA) of Pt-CoO@NPC@SnO$_2$-1 (88.19 m^2 g$_{Pt}^{-1}$) is higher than that of Pt/C (76.19 m^2 g$_{Pt}^{-1}$). The MOR catalytic activity of a catalyst is positively correlated with the peak intensity of the hydrogen adsorption/desorption region [3,8,12]. The bigger region of the hydrogen adsorption/desorption of Pt-CoO@NPC@SnO$_2$-1 is mainly attributed to the porous structure (high S$_{BET}$) of CoO@NPC@SnO$_2$-1 support with abundant exposed active sites [8]. As shown in Figs. 6e and S22, Pt-CoO@NPC@SnO$_2$-1 exhibits a high mass activity of 1518 mA mg$_{Pt}^{-1}$ at 0.78 V, which is far higher than those of Pt/C (496.8 mA mg$_{Pt}^{-1}$, 3.05 times) and Pt-CoO@NPC (406 mA mg$_{Pt}^{-1}$, 3.74 times). The mass activities of Pt-CoO@NPC@SnO$_2$-y (y = 0.5, 0.75, 1.25 and 1.5) are 573.12, 646, 1228 and 876 mA mg$_{Pt}^{-1}$, respectively. Summary of the MOR activities of CoO@NPC@SnO$_2$-1 and other recently-reported catalysts is listed in Table S3 [60–64]. The higher mass activity of Pt-CoO@NPC@SnO$_2$-1 for MOR is attributed to the strong metal-metal oxide interactions between SnO$_2$ and Pt, and the desirable co-catalytic activity of CoO@NPC@SnO$_2$-1 support

[13,31,33]. The contact chance between electrolyte and available Pt active sites is increased by loading Pt onto the 3d porous structure [31]. Importantly, SnO$_2$ in the CoO@NPC@SnO$_2$-1 may catalyze the decomposition of water to generate *OH (SnO$_2$-OH) to oxidize the small-molecule intermediates (poisons) existed on the adjacent Pt atoms [13,30,65].

CA measurements are applied to study the stability of Pt-CoO@NPC@SnO$_2$-1 for MOR. As shown in Fig. 6f, the current densities of Pt-CoO@NPC@SnO$_2$-1 and Pt/C fall rapidly within the first 400 s and then tend to stabilize. After 3600 s, the current density of Pt-CoO@NPC@SnO$_2$-1 is 445 mA mg$_{Pt}^{-1}$ (decline of 62.67%), which is far (3.15 times) higher than that of Pt/C (141 mA mg$_{Pt}^{-1}$, decline of 64.57%). The MOR stabilities of Pt-CoO@NPC@SnO$_2$-1 and Pt/C are further studied by ADTs. As shown in Fig. S23, at the 2500 and 5000 cycles, the peak current densities of Pt-CoO@NPC@SnO$_2$-1 retain 78.4 and 70.5% of its initial value, while the peak current densities of Pt/C retain 67.8 and 58.4%, respectively. The better durability of CoO@NPC@SnO$_2$-1
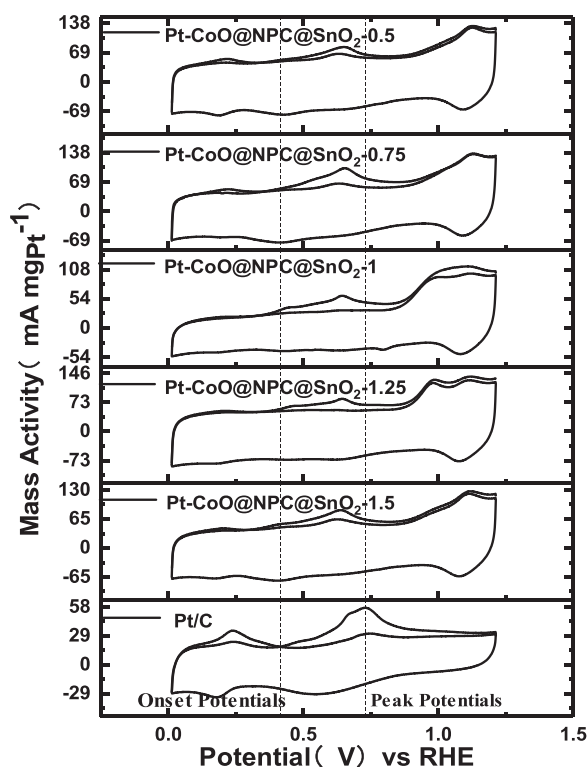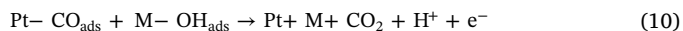
Fig. 7. CO stripping voltammograms of the Pt-CoO@NPC@SnO$_2$-y (y = 0.5, 0.75, 1, 1.25 and 1.5) and Pt/C catalysts.

should be attributed to the bigger specific surface area, and the improved charge transfer capacity and CO resistance [4]. Moreover, the N species in the carbon skeleton can alter the symmetric distribution of carbon-hexagon networks to generate defects to enhance electron transfer capacity to improve the durability and activity of MOR [8]. To further evaluate the CO poisoning resistance, CO stripping voltammograms tests for CoO@NPC@SnO$_2$ catalysts are carried out in 1 M KOH. As shown in Fig. 7 and Table S4, all of the onset and peak potentials of CO oxidation for CoO@NPC@SnO$_2$ catalysts are more negative than those of Pt/C, indicating that CoO@NPC@SnO$_2$ catalysts have better

CO tolerance/removal capacity during MOR. The better stability and CO tolerance capacity of Pt-CoO@NPC@SnO$_2$-1 are attributed to the co-catalytic activity of M (SnO$_2$/CoO), which can generate MOH to eliminate CO to recover Pt active sites for further oxidation of methanol through the following mechanisms (Eqs. (7)–(10)) [28,29]. The M (SnO$_2$ and/or CoO) can act as an active center for adsorption of OH$_{ads}$ at lower potentials to decrease the onset and peak potentials of CO oxidation [29].

$$Pt + CH_3 OH \rightarrow Pt - CH_3OH_{ads} \tag{7}$$

$$Pt - CH_3OH_{ads} + 4OH^- \rightarrow Pt - CO_{ads} + 4H_2 O + 4e^- \tag{8}$$

$$M + OH^- \rightarrow M - OH_{ads} + e^- \tag{9}$$

$$Pt - CO_{ads} + M - OH_{ads} \rightarrow Pt + M + CO_2 + H^+ + e^- \tag{10}$$

The Nyquist plots and the equivalent circuit diagram (inset) of CoO@NPC@SnO$_2$-y and Pt/C are shown in Fig. S24. As the amount of SnCl$_2$·2H$_2$O increases, the R$_{ct}$ of Pt-CoO@NPC@SnO$_2$ first decrease and then increase, consistent with the R$_{ct}$ results for ORR. The R$_{ct}$ of Pt-CoO@NPC@SnO$_2$-1 is the smallest one (7.46 Ω) among the as-prepared catalysts, which is much smaller than that of Pt/C (42.28 Ω), indicating that it can effectively reciprocate the charge transfer between catalyst and electrolyte to reduce the R$_{ct}$. As expected, the SnO$_2$ shells can effectively reduce the R$_{ct}$ to accelerate the charge transfer on Pt-CoO@NPC@SnO$_2$-1, thus improving its MOR catalytic activity [32].

3.4. ORR and MOR mechanisms

Fig. 8 shows the possible ORR and MOR mechanisms on CoO@NPC@SnO$_2$-1 and Pt-CoO@NPC@SnO$_2$-1, respectively. For ORR, the oxygen vacancies can effectively modify the electron structure of CoO@NPC@SnO$_2$-1 to optimize valence state of active sites, which thus obtain the rapid reaction kinetics [59]. Moreover, the N species in CoO@NPC@SnO$_2$-1 can promote the oxygen chemisorption through the polarization of carbon-hexagon networks [39]. The surface Co$_{Td}^{2+}$ from CoO can obtain full oxygen coordination with the oxygen of H$_2$O, meanwhile the H atoms of H$_2$O is distributed over the surface of CoO. The Co$_{Td}^{2+}$ may be reduced to fulfill charge-compensation of protonation of surface oxygen ligand, thereby generating the Co^{2+} − OH$^-$ species [24]. The Co^{2+} − OH$^-$ can further react with adsorbed O$_2$ with end-on and/or side-on bonding on CoO surfaces [24]. The SnO$_2$ also can absorb
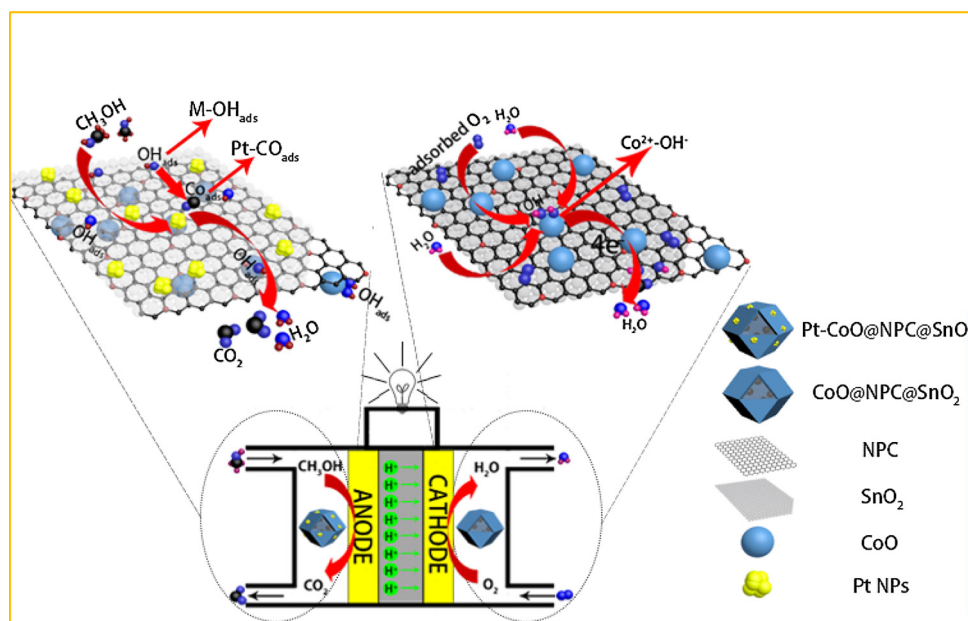

Fig. 8. Schematic illustration of possible ORR (using CoO@NPC@SnO$_2$ catalyst) and MOR (using Pt-CoO@NPC@SnO$_2$ catalyst) mechanisms.

OH⁻ species to improve the methanol poisoning resistance during ORR [7,9]. For MOR, because of the desirable interactions between Pt and SnO_2, the electronic structures of Pt are altered to improve the density of exposed active sites to enhance the MOR activity [13]. During MOR, SnO_2 shells and CoO cores can increase the concentration of OH⁻ species on the surface of Pt-CoO@NPC@SnO_2-1 through the adsorption of OH⁻ to generate the M-OH$_{ads}$ [28,29]. Through the efficient oxidation of CO$_{ads}$ on the Pt active sites by OH$_{ads}^-$, the dissociation-adsorption rate of methanol can be improved to increase the MOR activity [30]. The 3d porous structure can provide abundant internal available space for fast mass diffusion to improve ECSA and mass activity for MOR [4,8,13]. The synergistic effects among CoO, SnO_2, N species, and 3d porous polyhedron carbon can greatly improve the reactivity of active sites for MOR.

4. Conclusions

In summary, we synthesize the hierarchical CoO@NPC@SnO_2 polyhedrons originated from ZIF-67 as the highly active catalysts with promising methanol tolerances for ORR and as the Pt co-catalysts/supports with excellent CO tolerances for MOR via a two-step pyrolysis-oxidation strategy. CoO@NPC@SnO_2-1 exhibits the high ORR performance with promising peak potential (0.82 V), onset potential ($E_O = 0.95$ V), half-wave potential ($E_{1/2} = 0.83$ V), limiting current density ($J_L = -5.5$ mA cm^{-2}), stability ($\Delta E_{1/2} = 10$ mV, after 5000 cycles) and methanol tolerance. The high ORR activity is attributed to its special 3d core-shell structure, exposure of more active sites (CoO, N species and oxygen vacancies) and oxygen-containing functional groups. Moreover, the outer SnO_2 and NPC shells can prevent the CoO cores from corrosion and aggregation. For MOR, the Pt-CoO@NPC@SnO_2-1 (5 wt.%) shows the higher mass activity (1518 mA mg$_{Pt}^{-1}$), CO tolerance and stability, which can be attributed to the strong interactions between Pt and SnO_2. The formed M-OH$_{ads}$ species can remove the CO$_{ads}$ during MOR to enhance the charge transfer capacity and durability. Therefore, this work encourages us to provide more efforts for preparation of hierarchical double metal oxides catalysts for DMFCs by using ZIFs as templates.

Declaration of Competing Interest

The authors declare that they have no known competing financial interests or personal relationships that could have appeared to influence the work reported in this paper.

Acknowledgments

Appendix A. Supplementary data

Supplementary material related to this article can be found, in the online version, at doi:https://doi.org/10.1016/j.apcatb.2019.118043.

References

[1] J. Chang, L. Feng, C. Liu, W. Xing, X. Hu, Energy Environ. Sci. 7 (2014) 1628–1632.
[2] Y.L. Hsin, K.C. Hwang, C.-T. Yeh, J. Am. Chem. Soc. 129 (2007) 9999–10010.
[3] C. Zhang, Y. Dai, H. Chen, Y. Ma, B. Jing, Z. Cai, Y. Duan, B. Tang, J. Zou, J. Mater. Chem. A 6 (2018) 22636–22644.
[4] S. Kim, J.E. Park, W. Hwang, Y.-H. Cho, Y.-E. Sung, Appl. Catal. B: Environ. 209 (2017) 91–97.
[5] J.N. Tiwari, W.G. Lee, S. Sultan, M. Yousuf, A.M. Harzandi, V. Vij, K.S. Kim, ACS Nano 11 (2017) 7729–7735.
[6] L. Zhao, X.-L. Sui, J.-Z. Li, J.-J. Zhang, L.-M. Zhang, G.-S. Huang, Z.-B. Wang, Appl. Catal. B: Environ. 231 (2018) 224–233.
[7] H. Hu, L. Han, M. Yu, Z. Wang, X.W. Lou, Energy Environ. Sci. 9 (2016) 107–111.
[8] B. Tang, Y. Lin, Z. Xing, Y. Duan, S. Pan, Y. Dai, J. Yu, J. Zou, Electrochim. Acta 246 (2017) 517–527.
[9] D. Ding, K. Shen, X. Chen, H. Chen, J. Chen, T. Fan, R. Wu, Y. Li, ACS Catal. 8 (2018) 7879–7888.
[10] J. Masa, W. Xia, I. Sinev, A. Zhao, Z. Sun, S. Gruetzke, P. Weide, M. Muhler, W. Schuhmann, Angew. Chem. Int. Ed. 53 (2014) 8508–8512.
[11] A. Zhao, J. Masa, W. Xia, A. Maljusch, M.-G. Willinger, G. Clavel, K. Xie, R. Schloegl, W. Schuhmann, M. Muhlert, J. Am. Chem. Soc. 136 (2014) 7551–7554.
[12] Y. Sun, Y. Zhou, C. Zhu, L. Hu, M. Han, A. Wang, H. Huang, Y. Liu, Z. Kang, Nanoscale 9 (2017) 5467–5474.
[13] M. Huang, J. Zhang, C. Wu, L. Guan, ACS Appl. Mater. Interfaces 9 (2017) 26921–26927.
[14] Z. Hu, Z. Zhang, Z. Li, M. Dou, F. Wang, ACS Appl. Mater. Interfaces 9 (2017) 16109–16116.
[15] J.H. Song, C.Z. Zhu, B.Z. Xu, S.F. Fu, M.H. Engelhard, R.F. Ye, D. Du, S.P. Beckman, Y.H. Lin, Adv. Energy Mater. 7 (2017) 1601555.
[16] X. Huang, Y. Zhang, H. Shen, W. Li, T. Shen, Z. Ali, T. Tang, S. Guo, Q. Sun, Y. Hou, ACS Energy Lett. 3 (2018) 2914–2920.
[17] T. Qiu, Z. Liang, W. Guo, S. Gao, C. Qu, H. Tabassum, H. Zhang, B. Zhu, R. Zou, Y. Shao-Horn, Nano Energy 58 (2019) 1–10.
[18] B.Y. Xia, Y. Yan, N. Li, H.B. Wu, X.W. Lou, X. Wang, Nat. Energy 1 (2016) 15006.
[19] Z. Wang, Y. Lu, Y. Yan, T.Y.P. Larissa, X. Zhang, D. Wuu, H. Zhang, Y. Yang, X. Wang, Nano Energy 30 (2016) 368–378.
[20] Z. Guo, F. Wang, Y. Xia, J. Li, A.G. Tamirat, Y. Liu, L. Wang, Y. Wang, Y. Xia, J. Mater. Chem. A 6 (2018) 1443–1453.
[21] A. Aijaz, J. Masa, C. Roesler, W. Xia, P. Weide, A.J.R. Botz, R.A. Fischer, W. Schuhmann, M. Muhler, Angew. Chem. Int. Ed. 55 (2016) 4087–4091.
[22] J. Xiao, Q. Kuang, S. Yang, F. Xiao, S. Wang, L. Guo, Sci. Rep. 3 (2013) 2300.
[23] Y. Xue, S. Sun, Q. Wang, Z. Dong, Z. Liu, J. Mater. Chem. A 6 (2018) 10595–10626.
[24] X. Ge, A. Sumboja, D. Wuu, T. An, B. Li, F.W.T. Goh, T.S.A. Hor, Y. Zong, Z. Liu, ACS Catal. 5 (2015) 4643–4667.
[25] T. Kosmala, L. Calvillo, S. Agnoli, G. Granozzi, ACS Catal. 8 (2018) 2343–2352.
[26] W. Du, G. Yang, E. Wong, N.A. Deskins, A.I. Frenkel, D. Su, X. Teng, J. Am. Chem. Soc. 136 (2014) 10862–10865.
[27] S. St John, P. Boolchand, A.P. Angelopoulos, Langmuir 29 (2013) 16150–16159.
[28] A. Nouralishahi, A.M. Rashidi, Y. Mortazavi, A.A. Khodadadi, M. Choolaei, Appl. Surf. Sci. 335 (2015) 55–64.
[29] H. An, L. Pan, H. Cui, B. Li, D. Zhou, J. Zhai, Q. Li, Electrochim. Acta 102 (2013) 79–87.
[30] L. Nan, Z. Fan, W. Yue, Q. Dong, L. Zhu, L. Yang, L. Fan, J. Mater. Chem. A 4 (2016) 8898–8904.
[31] B. Ruiz-Camacho, H.H. Rodriguez Santoyo, J.M. Medina-Flores, O. Alvarez-Martinez, Electrochim. Acta 120 (2014) 344–349.
[32] N. Garino, A. Sacco, M. Castellino, J.A. Munoz-Tabares, A. Chiodoni, V. Agostino, V. Margaria, M. Gerosa, M. Quaglio, ACS Appl. Mater. Interfaces 8 (2016) 4633–4643.
[33] Z. Zhang, J. Liu, J. Gu, L. Su, L. Cheng, Energy Environ. Sci. 7 (2014) 2535–2558.
[34] Y. Guo, J. Tang, H. Qian, Z. Wang, Y. Yamauchi, Chem. Mater. 29 (2017) 5566–5573.
[35] L. Hu, G. Zhang, M. Liu, Q. Wang, P. Wang, Chem. Eng. J. 338 (2018) 300–310.
[36] X. Huang, J. Wang, H. Bao, X. Zhang, Y. Huang, 3D nitrogen, ACS Appl. Mater. Interfaces 10 (2018) 7180–7190.
[37] Y. Lin, J. Yu, Z. Xing, X. Guo, X. Yu, B. Tang, J. Zou, Electrochim. Acta 213 (2016) 341–350.
[38] H. Chen, S. You, Y. Ma, C. Zhang, B. Jing, Z. Cai, B. Tang, N. Ren, J. Zou, Chem. Mater. 30 (2018) 6014–6025.
[39] L. Yang, Z. Cai, L. Hao, Z. Xing, Y. Dai, X. Xu, S. Pan, Y. Duan, J. Zou, ACS Appl. Mater. Interfaces 9 (2017) 22518–22529.
[40] W. Shi, F. Guo, C. Zhu, H. Wang, H. Li, H. Huang, Y. Liu, Z. Kang, J. Mater. Chem. A 5 (2017) 19800–19807.
[41] P.G. Choi, N. Izu, N. Shirahata, Y. Masuda, ACS Appl. Nano Mater. 2 (2019) 1820–1827.
[42] A.L. Santos, D. Profeti, P. Olivi, Electrochim. Acta 50 (2005) 2615–2621.
[43] W. Ni, S. Liu, Y. Fei, Y. He, X. Ma, L. Lu, Y. Deng, ACS Appl. Mater. Interfaces 9 (2017) 14749–14757.
[44] R. Zhao, W. Xia, C. Lin, J. Sun, A. Mahmood, Q. Wang, B. Qiu, H. Tabassum, R. Zou, Carbon 114 (2017) 284–290.
[45] Y. Pei, Z. Qi, X. Li, R.V. Maligal-Ganesh, T.W. Goh, C. Xiao, T. Wang, W. Huang, J. Mater. Chem. A 5 (2017) 6186–6192.
[46] L. Wang, X. Jin, J. Fu, Q. Jiang, Y. Xie, J. Huang, L. Xu, J. Electroanal. Chem. 825 (2018) 65–72.
[47] R. Li, X. Wang, Y. Dong, X. Pan, X. Liu, Z. Zhao, J. Qiu, Carbon 132 (2018) 580–588.
[48] X. Wen, X. Yang, M. Li, L. Bai, J. Guan, Electrochim. Acta 296 (2019) 830–841.
[49] J. Guo, S. Gadipelli, Y. Yang, Z. Li, Y. Lu, D.J.L. Brett, Z. Guo, J. Mater. Chem. A 7 (2019) 3544–3551.
[50] J.-X. Zhang, L.-N. Zhou, J. Cheng, X. Yin, W.-T. Kuang, Y.-J. Li, J. Mater. Chem. A 7 (2019) 4699–4704.
[51] J. Chen, X. Yuan, F. Lyu, Q. Zhong, H. Hu, Q. Pan, Q. Zhang, J. Mater. Chem. A 7 (2019) 1281–1286.

[52] A. Kong, C. Mao, Q. Lin, X. Wei, X. Bu, P. Feng, Dalton Trans. 44 (2015) 6748–6754.
[53] X. Zhou, Y.-j. Gao, S.-w. Deng, S. Cheng, S.-h. Zhang, H. Hu, G.-l. Zhuang, X. Zhong, J.-g. Wang, Ind. Eng. Chem. Res. 56 (2017) 11100–11110.
[54] Z. Hu, Z. Guo, Z. Zhang, M. Dou, F. Wang, ACS Appl. Mater. Interfaces 10 (2018) 12651–12658.
[55] T. Hu, Y. Wang, L. Zhang, T. Tang, H. Xiao, W. Chen, M. Zhao, J. Jia, H. Zhu, Appl. Catal. B: Environ. 243 (2019) 175–182.
[56] M. Shi, X. Tong, W. Li, J. Fang, L. Chen, C.-a. Ma, ACS Appl. Mater. Interfaces 9 (2017) 34990–35000.
[57] M.-C. Tsai, N. Trung-Thanh, N.G. Akalework, C.-J. Pan, J. Rick, Y.-F. Liao, W.-N. Su, B.-J. Hwang, ACS Catal. 6 (2016) 6551–6559.
[58] A. Safakas, G. Bampos, S. Bebelis, Appl. Catal. B: Environ. 244 (2019) 225–232.

[59] H. Yuan, J. Li, W. Yang, Z. Zhuang, Y. Zhao, L. He, L. Xu, X. Liao, R. Zhu, L. Mai, ACS Appl. Mater. Interfaces 10 (2018) 16410–16417.
[60] G. Yuan, L. Wang, X. Zhang, Q. Wang, J. Colloid Interface Sci. 536 (2019) 189–195.
[61] Y. Zhang, Y. Liu, W. Liu, X. Li, L. Mao, Appl. Surf. Sci. 407 (2017) 64–71.
[62] M. Wang, X. Song, Q. Yang, H. Hua, S. Dai, C. Hu, D. Wei, J. Power Sources 273 (2015) 624–630.
[63] Y. Ren, S. Zhang, H. Fang, X. Wei, P. Yang, J. Energy Chem. 23 (2014) 801–808.
[64] C. Wang, L. Zheng, R. Chang, L. Du, C. Zhu, D. Geng, D. Yang, ACS Appl. Mater. Interfaces 10 (2018) 29965–29971.
[65] R.M. Antoniassi, J.C.M. Silva, A. Oliveira Neto, E.V. Spinace, Appl. Catal. B: Environ. 218 (2017) 91–100.